JSS Focus Issue on Properties, Devices, and Applications Based on 2D Layered Materials

Single-Layer Graphene Synthesis on a Al_2O_3(0001)/Cu(111) Template Using Chemical Vapor Deposition

Ken Verguts,[a,b,z] Nandi Vrancken,[b,c] Bart François Vermeulen,[b] Cedric Huyghebaert,[b] Herman Terryn,[c] Steven Brems,[b] and Stefan De Gendt[a,b,*]

[a]*Departement Chemie, Katholieke Universiteit Leuven, B-3001 Leuven, Flemish Brabant, Belgium*
[b]*imec vzw, B-3001 Leuven, Flemish Brabant, Belgium*
[c]*Departement Materialen en Chemie, Vrije Universiteit Brussel, B-1050 Brussels, Brussels, Belgium*

The parameter space of graphene growth using chemical vapor deposition on an untwinned single-crystalline Al_2O_3(0001)/Cu(111) template is discussed. The influence of growth temperature, methane flow and carbon dose is examined to assess graphene quality and multilayer coverage. An optimized growth window is identified yielding single-layer graphene. Production temperatures above 850°C result in a graphene quality improvement, but also an increase in multilayer coverage. Adapting graphene dosages by minimizing the growth time is the key element to reduce the amount of multilayer domains without affecting the quality. After graphene transfer, the multilayer graphene areas show a large increase in I_{2D}/I_G peak ratio, which indicates a turbostratic stacking order of graphene multilayer domains. Two growth models are put forward, i.e. a carbon penetration mechanism and an adsorption-diffusion mechanism.

Manuscript submitted July 5, 2016; revised manuscript received August 1, 2016. Published August 11, 2016. *This paper is part of the JSS Focus Issue on Properties, Devices, and Applications Based on 2D Layered Materials.*

Graphene, a 2D material[1,2] consisting of only carbon atoms arranged in a hexagonal pattern, exhibits a unique combination of outstanding properties: extremely high carrier mobility,[3] almost complete optical transparency,[4] superior thermal conductivity[5] and yet unmatched intrinsic strength.[6] The exceptional and unique features render graphene an ideal candidate for future nano-electronic applications, including sensors,[7] photodetectors[8] and flexible electronics.[9] Introduction of graphene in these fields requires a scalable production method yielding uniform high-quality graphene sheets. Many synthesis techniques are reported in literature, including mechanical[1] and chemical exfoliation,[10,11] chemical vapor deposition (CVD),[12] reduction of graphene oxide (GO)[13] and epitaxial growth on SiC.[14,15] To date, none of them has yielded an economically viable synthesis route for high-quality graphene. Chemical vapor deposition, using a carbon containing gas over single-crystalline transition metal templates, is amongst the most promising candidates to yield high-quality large area graphene sheets at low cost. Extensively studied candidate catalytic templates for CVD graphene growth are germanium,[16] nickel,[17] copper[18] and platinum.[19] The low carbon solubility in Cu[20] ensures a self-limiting process, driven by surface adsorption and should thus circumvents the problem of multilayer growth.[21] However, despite this low carbon solubility, bilayer graphene islands are still often observed.[22] The stacking order of the different layers could be divided in either Bernal-stacked (AB) graphene or the less studied turbostratic stacked (twisted) graphene. The difference between the two stacking orders can be assessed using Raman spectroscopy.

Bernal-stacked (AB) bilayer graphene is an interesting material because of its tunable bandgap of up to 250 meV by an external electric field.[23] This renders AB stacked graphene an ideal candidate for functional electronic and photonic devices. Another, less examined, stacking order of graphene layers is the turbostratic stacking.[24–28] In this case, two graphene layers are rotated with respect to each other by an angle of $\theta \neq n\ 60^\circ$ where $n = 0, 1, 2, \ldots$ This rotation can mitigate π-orbital hybridization, thus, restoring the electronic structure of monolayer graphene in a multilayer configuration.[29]

The formation mechanism of turbostratic bilayer graphene domains as a function of the different studied parameters is addressed by Raman spectroscopy after transfer to Si/SiO_2, as sensitivity requires this (see further). To assess the growth mechanism, one has to detect first if the second graphene layer grows on top of the first layer (see Figs. 1a–1b),[30–32] or between the first layer and the growth substrate (see Figs. 1c–1f).[33–38] The proposed mechanisms for graphene growth on top of the first graphene layer are known as the Frank-van der Werwe model[30,31] and the Volmer-Weber model.[32] In the Frank-van der Werwe model, clusters are formed since the second layer already grows before the first layer is closed, whereas the Volmer-Weber model describes the growth of the second layer after complete closure of the first layer. In the latter growth model, the catalytic

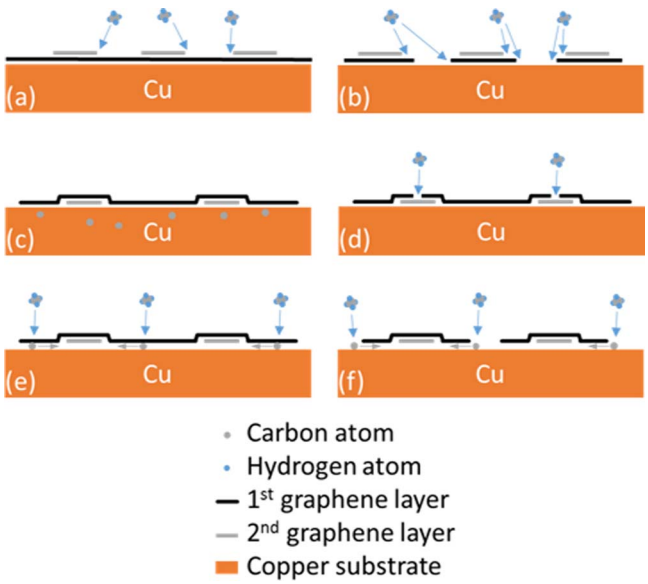

Figure 1. Six proposed mechanisms to evaluate bilayer growth. (a) Frank-van der Werwe model: the second layer grows on top of the first monolayer. (b) Volmer-Weber model: formation of multilayer islands. (c) Diffused carbon atoms segregate during cooling down, forming a second layer. (d) The carbon precursor reaches the catalyst through grain boundaries and defects in the first layer, forming the second layer. (e) Gas phase penetration mechanism. (f) Adsorption-diffusion mechanism.

*Electrochemical Society Fellow.
[z]E-mail: Ken.Verguts@imec.be

copper substrate is protected by the first graphene layer, which prevents further decomposition of methane molecules to form the second layer. This makes the latter growth model unlikely. Furthermore, Nie et al.[39] performed a study on the relative position of the different layers using low-energy electron diffraction (LEED) and low-energy electron microscopy (LEEM) to conclude that the bilayer domains indeed nucleate from below. Therefore, the top graphene growth models are improbable in our growth process.

Several models are also put forward to explain the graphene growth in between graphene and the catalyst substrate. In a first model, dissolved carbon species segregate to the surface upon cooling, forming the second layer (see Fig. 1c).[33] However, this mechanism applies only for metals with a high carbon solubility (e.g. nickel). Since the carbon solubility in Cu is extremely low (0.008 wt% at 1084°C),[20] this mechanism is unlikely. The remaining models describes the growth of a second layer through defects and grain boundaries of the first layer (see Fig. 1d),[34] through a carbon exchange mechanism (see Fig. 1e)[35] and carbon diffusion and intercalation at the edges of a monolayer (see Fig. 1f).[36] It is reported that the last mechanism is very dependent on hydrogen partial pressures.[38] This behavior can be explained taking into account the graphene edge termination. At low hydrogen pressure, the graphene edges are directly passivated by the Cu surface. At high hydrogen pressure, graphene edges are terminated by hydrogen. The metal-passivated carbon atoms are active for C adsorption, which will grow the graphene monolayer. However, carbon monomers can easily diffuse underneath the graphene sheet and form a second graphene layer when the top graphene layer is hydrogen passivated. The formation of bilayer graphene as a function of parameters studied in our growth study and in view of the different models will be discussed at the end of this paper.

Experimental

Preparation of the Al_2O_3(0001)/Cu(111) template.—The Al_2O_3(0001)/Cu(111) template preparation is similar to that previously reported.[40] Pre-cut and polished 2″ Czochralski grown sapphire wafers (Roditi International Corporation) diced along the c-plane are used. The substrate wafers are monocrystalline with a surface misorientation of $\leq 0.3^\circ$. The sapphire wafers are cleaned using a 3:1 concentrated acid mixture of H_2SO_4:H_3PO_4 at 300°C for 20 min, followed by a 3 min ultrapure water (UPW) rinse. The acid clean removes the polishing scratches and leaves the sapphire surface Al-terminated. The subsequent UPW rinse hydroxylates the surface, which results in an OH-termination. The cleaned sapphire substrates are mounted on a dummy Si 200 mm wafer and transferred immediately to the Cu sputter deposition chamber (Nimbus 310 sputtering setup with a base pressure of 4×10^{-6} mbar). Sputtering is performed at room temperature for 173 s (21 passes under target) under 6×10^{-3} mbar Ar pressure. The applied power density is 4.7 W cm^{-2} (total applied power is 3000 W), and the throw distance is approximately 50 mm. This results in the formation of a twinned Cu(111) texturing.[40]

Synthesis of single-layer graphene on Al_2O_3(0001)/Cu(111).—The as-grown Al_2O_3(0001)/Cu(111) template was transferred to a commercial CVD system (6″ Aixtron Black Magic CVD system). Graphene synthesis was carried out using a reference process, where every parameter was kept constant except for one variable.

In a typical process at 90 mbar, native cuprous oxide was reduced using a flow of 40 sccm H_2, diluted in 960 sccm Ar. Simultaneously, the sample temperature was raised to about 1025°C which transforms the twinned Cu(111) layer into an untwinned layer.[40] The reduction is followed by graphene growth at the same temperature through the addition of the methane (CH_4) precursor for 30 min, without altering the H_2 and Ar flows. Next, the reactor chamber was cooled down to room temperature at a cooling rate of 10°C min^{-1}. Following parameters were varied in this study: the growth temperature, the growth time, the CH_4 flow and the influence of hydrogen (ranges will be addressed in the results section). The temperature profile is measured using K-type thermocouples connected directly to the top- and bottom heater.

Graphene transfer to Si/SiO_2 (90 nm).—Following growth, graphene can be transferred from the Al_2O_3(0001)/Cu(111) growth template onto SiO_2 substrates using a wet transfer procedure similar to that of Suk et al.[41] First, 3% PMMA in chlorobenzene was spin coated at 4500 rpm for 40 s and cured on a hotplate at 120°C for 30 s. Cu was etched in a 0.1 M $(NH_4)_2S_2O_8$ solution, and the graphene/PMMA stack was rinsed in UPW. Graphene/PMMA was wet transferred onto chips of nominal 90 nm SiO_2 wafer piece and heated to 45°C until dry. Afterwards, the wafer piece was baked for 10 min at 160°C, PMMA was removed from graphene in hot acetone (40°C) overnight, dipped in isopropanol and the transferred graphene was dried in a stream of nitrogen.

Characterization.—Optical microscopy is an efficient tool to quickly visualize and identify graphene on a substrate. However, visualization of monolayer and bilayer graphene domains is only possible after transfer to Si/SiO_2 (with an oxide thickness of 90 nm or 280 nm)[42,43] substrates, due to the very low optical contrast on copper substrates. To study the quality of a graphene monolayer as a function of different growth parameters, graphene was visualized after transfer using the contrast difference between multilayer and monolayer regions. Images were digitalized using MATLAB software and processed to quantify the amount of multilayer areas and nucleation density (given in 1000 nucleation sites per mm^2).

Raman spectroscopy is a powerful non-destructive tool used for graphene characterization[44] and is implemented to investigate the number of graphene layers (I_{2D}/I_G peak ratio), to characterize graphene doping and strain (change in Raman peaks shift)[45] and to evaluate the amount of sp^3-hybridized carbon atoms in the graphene sheet (I_D/I_G peak ratio). Since graphene only consists of sp^2-hybridized carbon atoms, graphene quality is inversely proportional with the intensity ratio of the Raman D- over G-peak.[46] Graphene is characterized using Raman spectroscopy (Horiba Labram HR with a green laser (λ = 532 nm), recording intensities from $\bar{\nu} = 1200$ cm^{-1} to $\bar{\nu} = 3300$ cm^{-1}). Three characteristic graphene peaks were examined: D-mode ($\sim$1350 cm^{-1}), G-mode ($\sim$1580 cm^{-1}) and 2D-mode ($\sim$2700 cm^{-1}). Graphene Raman peaks were fitted in MATLAB using a Lorentzian function. Peak intensities (i.e. I_D, I_G and I_{2D}), peak positions and full width at half maximum (FWHM) values were extracted. Raman spectroscopy can also differentiate between the two types of stacking order (i.e. AB-stacked vs. turbostratic stacked graphene).[27,46] Raman signals, obtained from turbostratic stacked graphene areas on Si/SiO_2, are similar to single-layer graphene, showing a sharp 2D-peak with an increased I_{2D}/I_G peak ratio of about 2.[27] These twisted bilayer domains can be clearly distinguished from AB stacked graphene since the 2D band for the latter consists of four components and shows a decreased I_{2D}/I_G peak ratio below 1.[46]

The graphene morphology was inspected using non-contact atomic force microscopy (AFM) in tapping mode (Bruker) and data was analyzed with Gwyddion.[47]

Results and Discussion

Effect of copper oxidation.—Non-controlled oxidized copper regions are often observed in both optical and scanning electron microscopy (SEM) as well as in atomic force microscopy (AFM) imaging (see white arrows in Figure 2). Also graphene bilayer domains are distinguished from single-layer graphene, using SEM and AFM phase imaging (see black arrows in Figure 2).

Intensities of the Raman active G- and 2D-peak are very much influenced by the Cu substrate.[48] In addition, graphene doping by the Cu substrate is strongly influenced over time as a result of copper template oxidation after growth.[49] This is shown by Raman analysis during a controlled Cu oxidation experiment (see Fig. 3a). Cu oxidation was accelerated by heating the sample on a hot plate at 120°C in ambient conditions and subsequently transferred to a Raman setup to study the

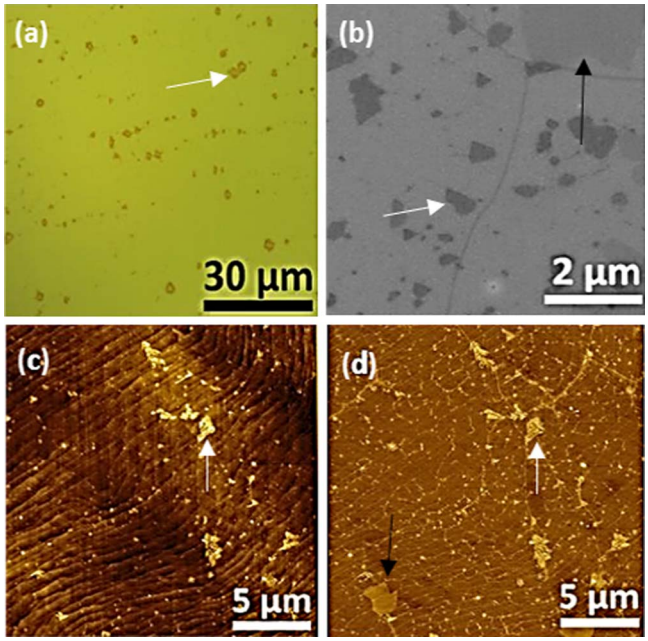

Figure 2. Optical (a), SEM (b), AFM height (c) and AFM phase (d) image of as-grown graphene. White arrows show the presence of oxidized copper regions whereas black arrows point to bilayer areas.

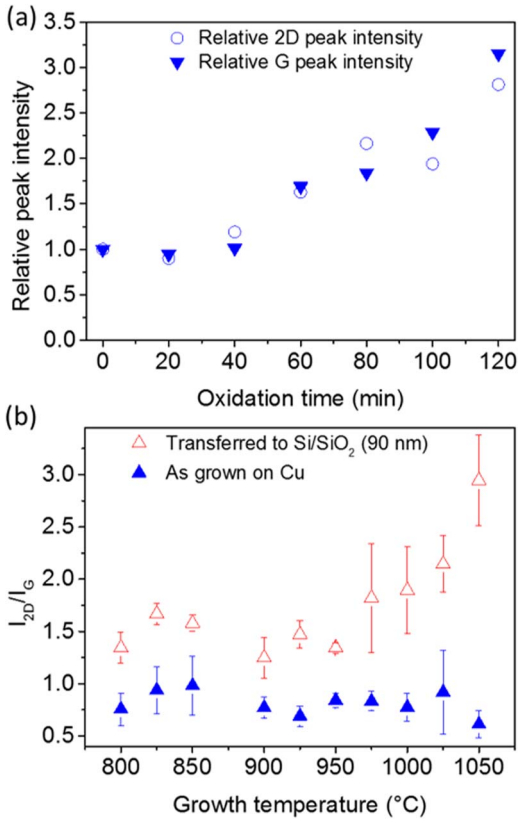

Figure 3. (a) Effect of G-peak (solid triangles) and 2D-peak (open circles) Raman intensity as a function of copper oxidation time. An increase in intensity is clearly observed for both peaks with increasing oxidation time. (b) Influence of the graphene growth temperature on I_{2D}/I_G of as-grown graphene on copper (solid triangles) and transferred graphene (open triangles). The I_{2D}/I_G peak ratio of graphene on copper remains unchanged whereas the I_{2D}/I_G peak ratio of transferred graphene increases with growth temperature.

influence of Cu oxidation on the different characteristic Raman features. With increasing oxidation time, an increase in G- and 2D-peak intensity is observed by a factor of about 3 (normalized against the G- and 2D-peak at $t_{oxidation} = 0$ min). Broadening of both peaks and a redshift upon oxidation was found (i.e. ~10 cm^{-1} (G) and ~48 cm^{-1} (2D), data not shown), which is in accordance to similar experiments performed by Yin et al.[49] It can be concluded that the presence of a partially oxidized copper/graphene interface hampers the analysis of as-grown graphene due to this uncontrolled Cu oxidation process, mandating the transfer process.

After transfer to Si/SiO_2, the influence of the growth temperature on the I_{2D}/I_G peak ratio is observed (see Fig. 3b). The I_{2D}/I_G peak ratio remains constant until approximately 950°C and increases at higher growth temperatures for graphene samples transferred to Si/SiO_2 (see Fig. 3b), indicating an improved graphene quality.[46,50] However, the clear trend in I_{2D}/I_G peak ratio as a function of the temperature is completely masked on the as-grown samples on copper, due to doping of the graphene sheet by the Cu(111) substrate. To avoid drawing wrong conclusions due to copper and partially oxidized copper substrate effects, graphene is transferred to Si/SiO_2 substrates. Therefore, Raman data of graphene on $Al_2O_3(0001)/Cu(111)$ are not reported in the article.

It has to be taken into account that polymers, used during the transfer process, are not removed completely in acetone. As a consequence, PMMA residues are left behind.[51] The amount of PMMA residues is proportional to defects in the graphene sheet. At increased growth temperatures, less high-energy sites (defects) are present, resulting in less p-doping caused by PMMA.[52] This link between doping and I_{2D}/I_G peak ratio was previously reported by Casiraghi[53] and Das et al.[54]

Influence of the growth temperature.—In order to obtain a high-quality monolayer graphene sheet without any bilayer areas on a $Al_2O_3(0001)/Cu(111)$ template, several growth parameters were examined. At first, the influence of the temperature on graphene growth is discussed. A starting recipe was chosen with following fixed flow rates during the graphene growth step: 10 sccm CH_4, 40 sccm H_2 and 960 sccm Ar at 90 mbar. Methane was introduced in the chamber at different temperatures for 30 min, corresponding to a total methane dose of 13.4 mmol for each experiment. A temperature window between 800°C and 1050°C was examined. Temperatures above 1050°C resulted in extensive Cu evaporation, which impacts the stability of the Cu(111) thin film. In Figure 4a, the Raman I_D/I_G peak ratios are given as well as the Raman shift and full width at half maximum (FWHM) of the 2D peak.

Data of the Raman G peak shift and FWHM are not influenced significantly in the temperature range studied, and are therefore not shown. The I_D/I_G peak ratio is relatively low at growth temperatures starting from 850°C and decreases below 0.1 at growth temperatures above 975°C, which indicates the formation of high quality graphene. For growth temperatures below 850°C, a drastic increase in I_D/I_G peak ratio is observed, which implies a more defective graphene sheet (see Fig. 4a). In addition, an increasing I_D/I_G peak ratio is also seen at growth temperatures above 1050°C, which corresponds with excessive Cu evaporation (data not shown). At the higher growth temperatures, a FWHM sharpening of the 2D-peak is observed while no trend is visible in the 2D-peak position (see Fig. 4b).

The influence of the growth temperatures on the average multilayer coverage as well as the multilayer nucleation density is shown in Figure 5 and a selection of corresponding optical images are depicted in Figure 6. A clear trend in multilayer coverage is observed with respect to the growth temperature. Below 875°C, only monolayer graphene is observed. Above 900°C, few bilayer islands appear, but the total bilayer coverage remains below 1%. At growth temperatures above 950°C, the average multilayer coverage raises to about 20%. The nucleation density as a function of the growth temperature shows a maximum around 1000°C. This multilayer density depends on the relative rates of nucleation and growth processes and on the competition between these processes.[55] It is expected that at temperatures

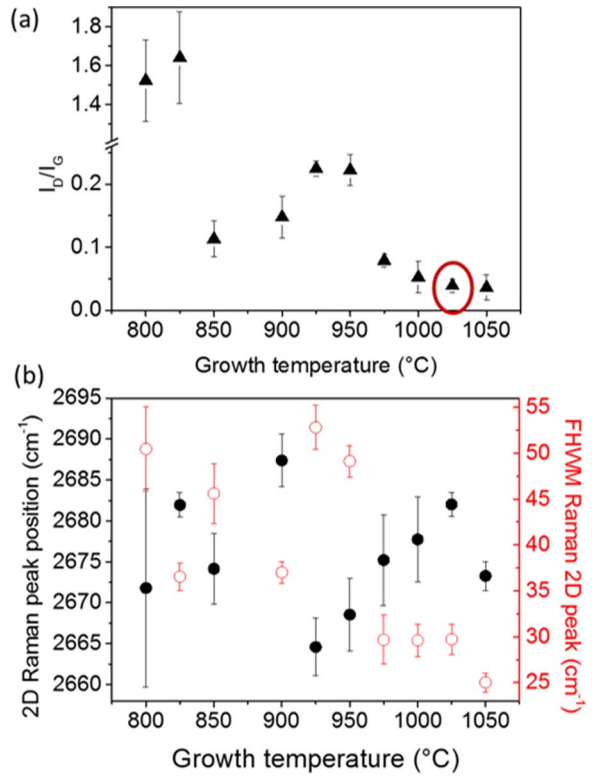

Figure 4. Influence of the graphene growth temperature on different Raman features after graphene transfer: (a) D/G intensity ratio (the red ellipse represents the same growth conditions as used in the next paragraph), (b) 2D Raman peak position (solid circles) and full width at half maximum (FWHM) of the 2D-peak (open circles).

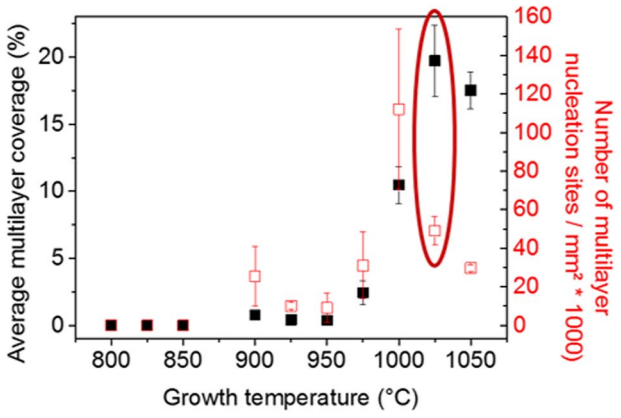

Figure 5. Average multilayer coverage and average number of multilayer nucleation sites of graphene as a function of the growth temperature. The red ellipse represents the same growth conditions as used in the next paragraph.

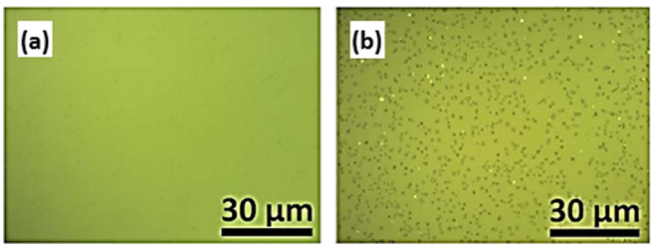

Figure 6. Optical images of graphene transferred to Si/SiO_2 (90 nm) and grown at a different growth temperature: 800°C (a) and 1000°C (b).

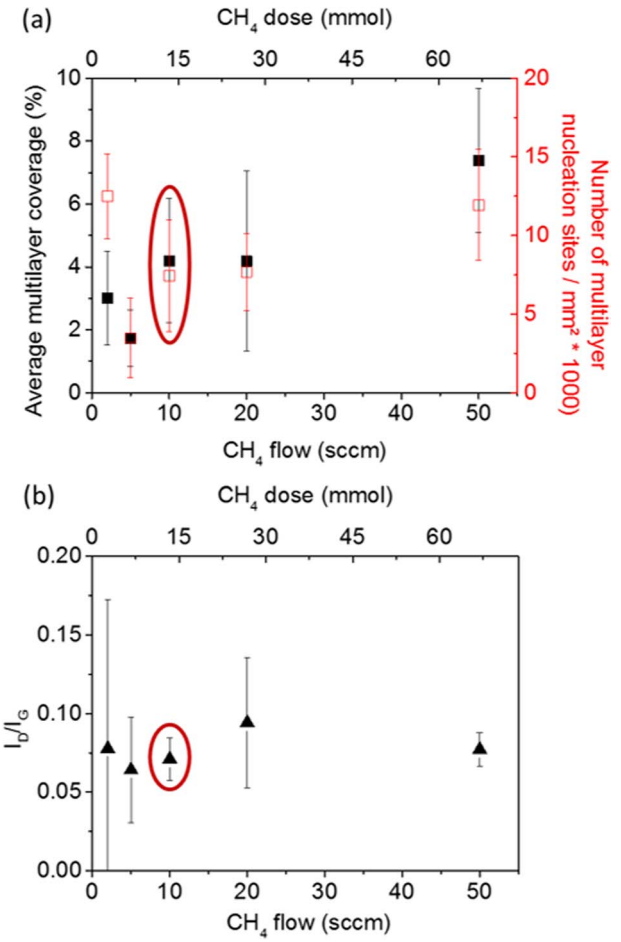

Figure 7. (a) Influence of the methane flow on the average multilayer coverage (solid squares) and the average number of nucleation sites (open squares). The carbon flow is varied from 2 sccm to 50 sccm. (b) Influence of the methane flow on the I_D/I_G peak ratio. The red ellipses represent the same growth conditions as used in the previous paragraph.

above 1000°C, the growth rate is higher than the nucleation rate, which explains the drop in multilayer nucleation density.

Influence of the methane flow at a fixed growth time and fixed methane/hydrogen ratio.—Following the temperature dependence experiments, graphene grown at a temperature of 1025°C possesses a low I_D/I_G peak ratio combined with a stable Cu(111) thin film. This means that with the given process the highest quality graphene sheet could be obtained at these growth temperatures. However, if the corresponding graphene multilayer coverage is assessed, it is observed that about 20% of the sample is covered with bilayer graphene. In order to reduce this multilayer coverage, the next parameter varied was the methane flow at a fixed growth temperature of 1025°C and a reactor pressure of 90 mbar with a growth time of 30 min. Hydrogen flow was adapted to preserve a CH_4/H_2 ratio of 0.25. Also the Ar flow was changed as such to maintain a constant total gas flow of 1000 sccm.

Raman measurements do not show any significant trend upon varying the methane dose (see Fig. 7b). Despite lowering the methane dose (range from 67 mmol to 3 mmol), only a small decrease in graphene multilayer coverage is observed at lower methane doses (see Fig. 7a). However, it should be noted that the error range is large, but in the range studied, the methane dose seems to have only a marginal influence.

Influence of the methane/hydrogen ratio.—Hydrogen flow is known to be a very important parameter in CVD graphene growth,

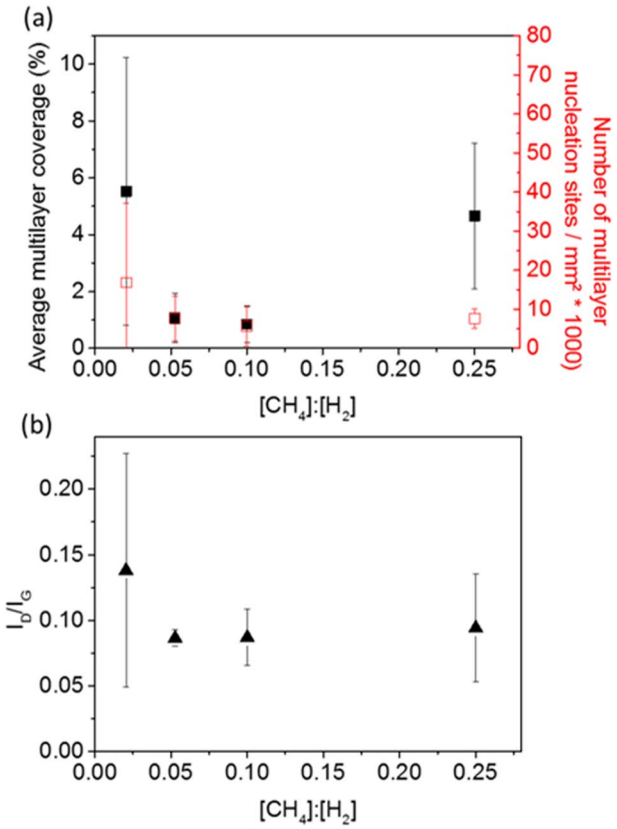

Figure 8. (a) Influence of the methane to hydrogen ratio on the average multilayer coverage (solid squares) and the average number of nucleation sites (open squares). The sum of both flows was kept constant at 100 sccm and the ratio was changed from 0.025 to 0.25. (b) Influence of the methane to hydrogen ratio on the I_D/I_G peak ratio.

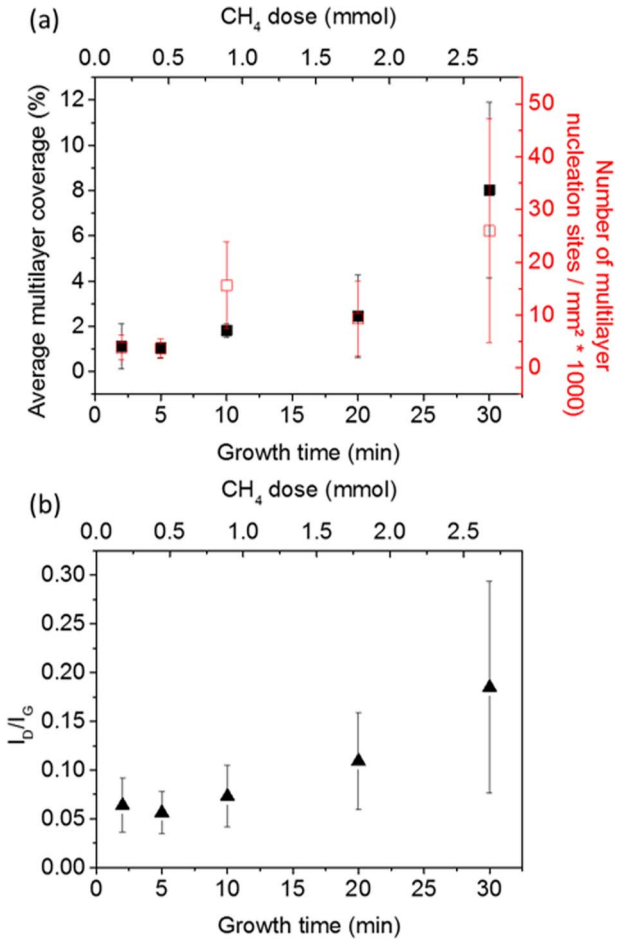

Figure 9. (a) Influence of the growth time on the average multilayer coverage (solid squares) and the average number of nucleation sites (open squares). The carbon flow was kept constant at 10 sccm, whereas the growth time has varied from 2 min to 30 min. (b) Influence of the growth time on the Raman I_D/I_G peak ratio.

although controversial in graphene literature.[56,57] It is known to etch graphene, but it is also supposed to act as a co-catalyst in the decomposition of methane.[58] Therefore, low methane to hydrogen ratios are expected to result in excessive methane decomposition and graphene etching, yielding a non-uniform graphene layer with reduced grain sizes, increased defectivity and many multilayer domains.[57–59] However, hydrogen also tends to etch sp^3-hybridized carbon atoms, present at defects, nucleation sites and grain boundaries, which increases the overall quality in the graphene sheet. Seifert et al.[60] reported larger domain size and a decrease in bilayer coverage upon decreasing the CH_4/H_2 ratio, whereas Vlassiouk et al.[56] even argued that CH_4/H_2 ratios of about 1/200 to 1/400 are necessary to achieve single-crystal, large-scale graphene islands. In fact, there should be an optimal CH_4/H_2 ratio which is in equilibrium with methane decomposition on the one hand and defect etching on the other hand.

To study the influence of the methane to hydrogen flow ratio, samples were grown at 1025°C for 30 min at a reactor pressure of 90 mbar. The sum of methane and hydrogen flow was fixed at 100 sccm with an Ar flow of 900 sccm. The hydrogen flow was varied between 98 sccm and 80 sccm.

The flow rates also do not clearly influence the amount of multilayer coverage, nor the nucleation density (see Fig. 8a). However, it should be noted that large error bars are only observed at intermediate methane to hydrogen ratios. Therefore, small deviations in nucleation behavior could be masked. Regarding the I_D/I_G peak ratio over the full set of measurements (see Fig. 8b), the graphene quality seems unaffected. Also no significant variation in I_{2D}/I_G peak ratio, Raman shift and FWHM of G- and 2D-peak could be observed (data not shown).

These observations might be explained by the fact that hydrogen was already introduced in the chamber during the temperature ramping phase. Therefore, the Cu layer was saturated already with hydrogen prior to graphene growth. However, we assume that this effect is rather negligible because the Cu(111) layer is very thin (500 nm) and has a low hydrogen solubility.[61] Furthermore, also the other parameters influence graphene growth conditions (i.e. methane flow, growth temperature and time).

Influence of the growth time (carbon dosing).—Regarding the previous paragraphs, carbon dosing was in the range of 2 mmol and 70 mmol, and only limited variation in multilayer coverage was observed. Therefore, it is assumed that the carbon dose in the range studied, is in a saturation regime, and has to be reduced further to study its influence. Therefore, the methane flow is reduced from 0.45 mmol min^{-1} (10 sccm, as used in previous experiments) to 0.09 mmol min^{-1} (2 sccm). In addition, the methane dose was varied by changing the growth time. Methane was introduced at a growth temperature of 1025°C and the flow rates were fixed at 2 sccm CH_4, 98 sccm H_2 and 900 sccm Ar, with a background pressure of 90 mbar. The growth time, i.e. the time span where methane is introduced to the reactor chamber, was varied between 2 min and 30 min, resulting in a methane dose in the range of 0.25 mmol tot 3 mmol.

Figure 9a shows the multilayer coverage and nucleation density as a function of growth time/carbon dose. A clear trend in multilayer coverage could be observed by analyzing the optical images of transferred graphene (see Fig. 10). A decrease in growth time (dose) clearly results in a decrease in multilayer coverage. The graphene

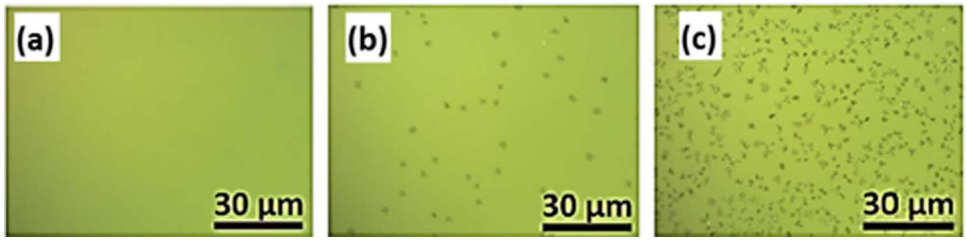

Figure 10. Optical images of the influence of the carbon precursor dose on the average multilayer coverage. The growth time was 45 s (a), 10 min (b) and 30 min (c).

quality is given by the I_D/I_G peak ratio (see Fig. 9b). A decrease in I_D/I_G peak ratio is observed for growth times up to 5 min, indicating an increase in graphene quality and crystallinity with decreasing growth time (dose). However, this I_D/I_G peak ratio increases again at higher methane doses, suggesting a more defective graphene sheet.[62] It can be concluded that minimizing the carbon dose is a key parameter in obtaining large scale high-quality monolayer graphene.

To evaluate the effect of methane dose, 2 sccm methane was introduced for only 10 s in the reactor chamber, corresponding to a methane dose of only 0.07 mmol (i.e. introducing the lowest CH_4 dosage possible in the graphene growth tool). Optical imaging, SEM and AFM analyses indicate that graphene sheets were already completely closed after such a low dose experiment. It was therefore not possible to investigate monolayer graphene nucleation and domain growth. Longer growth times do not yield graphene of a better quality, but result in an increase of multilayer coverage. Considering this extremely fast closure, a large nucleation density is expected. Investigation of the nucleation of monolayer grains is only feasible with even lower methane doses, i.e. shorter growth times (<10 s) and/or lower CH_4 flows (<2 sccm).

Turbostratic graphene domains.—In summary: samples grown above 900°C with a carbon dose of at least 0.2 mmol showed the presence of multilayer domains. The stacking order of the different layers could be determined using Raman spectroscopy with the laser focused on these multilayer islands. Bilayer domains are generally characterized by a lower I_{2D}/I_G peak ratio compared to monolayer graphene.[46] However, an interesting observed feature was the presence of a very large I_{2D}/I_G peak ratio (i.e. above 2) compared to the I_{2D}/I_G peak ratio of about 1.4 in monolayer graphene (see Fig. 11).

This strong intensity enhancement suggests an electronic coupling, due to a constructive quantum interference between the layers. However in AB-stacked bilayer graphene, the I_{2D}/I_G peak ratio decreases compared to monolayer.[46] Therefore, the layers cannot be AB-stacked.

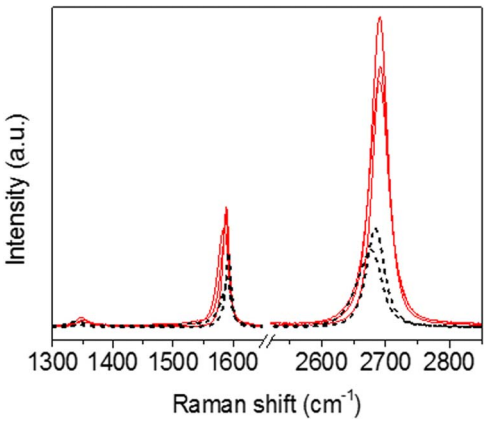

Figure 11. Raman spectra measured directly on bilayer domains (red solid curves) and measured on monolayer domains for comparison (black dashed curves).

A strong enhancement of the 2D-peak is observed before in the case of turbostratic stacked graphene with relatively high rotation angles.[63,64]

Multilayer stacking and growth mechanism.—Valuable data describing the multilayer graphene coverage and multilayer density could be extracted from the optical images after transfer. The influence of the different studied parameters provide a good insight in the nucleation and growth mechanism of the turbostratic stacked multilayer domains. To examine the origin of these multilayer domains, several mechanisms are suggested in literature (see Fig. 1) and will be discussed hereafter.

The Frank-van der Werwe model (see Fig. 1a),[30,31] is impossible, since the monolayer is already closed before the second layer with graphene nucleation centers appear. It is also observed that the multilayer nucleation density increases for longer growth times, suggesting secondary nucleation is taking place. The Volmer-Weber model (see Fig. 1b)[32] is unlikely since the catalytic copper substrate is protected by the first graphene layer, which prevents further decomposition of methane molecules to form the second layer. Moreover, the presence of a second layer on top of the first one would suggest a faster etching rate in hydrogen atmosphere. Therefore, we expect the top graphene growth models to be very unlikely in our growth process, as confirmed by Nie et al.[39]

Three models are able to describe the growth of a second graphene layer in between the existing graphene layer and the Cu catalyst layer. The first model describes the growth of a second layer through defects and grain boundaries of the first layer (see Fig. 1d).[34] Since graphene grain boundaries are definitely present due to the high graphene nucleation density, this model cannot be excluded. The second model is the carbon penetration through an exchange mechanism (see Fig. 1e),[35] and the third model is carbon diffusion and intercalation at the edges of a monolayer (see Fig. 1f).[36] The observed trend in multilayer coverage as a function of growth temperature suggests an interplay of the latter two mechanisms. However, both mechanisms have different activation energies. The former mechanism has a calculated theoretically activation energy of about 0.93 eV,[35] while the activation energy for the latter mechanism has not been reported to date, but is expected to be slightly higher than the activation energy for carbon diffusion on Cu (0.1 eV).[37]

At low growth temperatures, no bilayers are observed at all since the thermal energy of the active carbon species is too low to intercalate in between the growing graphene domains or to penetrate the monolayer. At higher growth temperatures (between 900°C and 950°C), bilayer graphene starts to form via the mechanism with the lowest activation energy (carbon diffusion and intercalation). This results in only small graphene bilayer domains, since the mechanism cannot continue when the first monolayer is completely closed. Experiments with very short growth times (<1 min) at 950°C already yielded complete monolayer coverage.

At even higher growth temperatures (>950°C), also the penetration mechanism becomes active, initially resulting in an increase in nucleation density and bilayer coverage. Eventually, the multilayer coverage levels off at very high temperatures due to the interplay between nucleation and growth. Higher temperatures favor growth owing to the higher mobility. In contrast, nucleation is favored at

lower temperatures (though high enough regarding the activation energy barrier) because of the higher driving force for crystallization.

Regarding the observed very fast growth rate of the first monolayer at temperatures around 1025°C, the carbon intercalation mechanism likely only contributes to a small extend to the multilayer formation. Moreover, it cannot explain the increase in multilayer nucleation density for the prolonged growth times as no new nucleation takes place once the copper is fully covered. Secondary nucleation requires penetration of the closed monolayer. The formation of bilayer domains underneath the monolayer sheet is in agreement with the experimental observation that multilayer coverage and nucleation density is rather independent of hydrogen concentration. Additionally, Wu et al.[35] investigated this penetration mechanism by first-principle calculations and pointed out that penetration of the formed bilayer domain is energetically unfavorable (energy barrier ≈3 eV), thereby inhibiting trilayer graphene growth. This matches with the experimental observation of extensive multilayer nucleation, but with only very limited trilayer coverage (<0.5%).

Conclusions

To conclude, the parameter range to obtain quality single-layer graphene growth was explored. With increasing quality – the bilayer areas showed a large increase in I_{2D}/I_G peak ratio which indicates a turbostratic stacking order. Moreover, a clear trend in multilayer growth can be observed by varying the growth temperature and the growth time. A growth temperature above 850°C results in a quality improvement as demonstrated by the large reduction of the Raman active D-peak, but also the multilayer coverage increases. Reducing the growth time (carbon dose) results both in a decreased multilayer coverage and an increased graphene quality. Due to tool limitations, the growth time could not be reduced further and a sub-monolayer graphene sheet was not obtained. The experimental data were put in perspective to some of the multilayer growth models and the multilayer nucleation could be explained by a combination of a penetration mechanism and an adsorption-diffusion mechanism.

Acknowledgments

We acknowledge K. Teo and B. Chen (Aixtron) for their support concerning graphene growth. This research was funded by a Ph.D. grant of the Agency for Innovation by Science and Technology (IWT), the EU Graphene Flagship and supported by imec's Core Partner Program.

References

1. K. S. Novoselov, A. K. Geim, S. V. Morozov, D. Jiang, Y. Zhang, S. V. Dubonos, I. V. Grigorieva, and A. A. Firsov, *Science*, **306**, 666 (2004).
2. K. S. Novoselov, D. Jiang, F. Schedin, T. J. Booth, V. V Khotkevich, S. V Morozov, and A. K. Geim, *Proc. Natl. Acad. Sci. U. S. A.*, **102**, 10451 (2005).
3. K. I. Bolotin, K. J. Sikes, Z. Jiang, M. Klima, G. Fudenberg, J. Hone, P. Kim, and H. L. Stormer, *Solid State Commun.*, **146**, 351 (2008).
4. R. R. Nair, P. Blake, A. N. Grigorenko, K. S. Novoselov, T. J. Booth, T. Stauber, N. M. R. Peres, and A. K. Geim, *Science*, **320**, 1308 (2008).
5. A. A. Balandin, S. Ghosh, W. Bao, I. Calizo, D. Teweldebrhan, F. Miao, and C. N. Lau, *Nano Lett.*, **8**, 902 (2008).
6. C. Lee, X. Wei, J. W. Kysar, and J. Hone, *Science*, **321**, 385 (2008).
7. J. T. Robinson, F. K. Perkins, E. S. Snow, Z. Wei, and P. E. Sheehan, *Nano Lett.*, **8**, 3137 (2008).
8. F. Xia, T. Mueller, Y.-M. Lin, A. Valdes-Garcia, and P. Avouris, *Nat. Nanotechnol.*, **4**, 839 (2009).
9. G. Eda, G. Fanchini, and M. Chhowalla, *Nat. Nanotechnol.*, **3**, 270 (2008).
10. M. Lotya, Y. Hernandez, P. J. King, R. J. Smith, V. Nicolosi, L. S. Karlsson, F. M. Blighe, S. De, W. Zhiming, I. T. McGovern, G. S. Duesberg, and J. N. Coleman, *J. Am. Chem. Soc.*, **131**, 3611 (2009).
11. M. Lotya, P. J. King, U. Khan, S. De, and J. N. Coleman, *ACS Nano*, **4**, 3155 (2010).
12. C. Oshima and A. Nagashima, *J. Phys. Condens. Matter*, **9**, 1 (1997).
13. D. R. Dreyer, S. Park, C. W. Bielawski, and R. S. Ruoff, *Chem. Soc. Rev.*, **39**, 228 (2010).
14. S. Tanaka, R. S. Kern, R. F. Davis, J. F. Wendelken, and J. Xu, *Surf. Sci.*, **350**, 247 (1996).
15. T. Tsukamoto, M. Hirai, M. Kusaka, M. Iwami, T. Ozawa, T. Nagamura, and T. Nakata, *Surf. Sci.*, **371**, 316 (1997).
16. J.-H. Lee, E. K. Lee, W.-J. Joo, Y. Jang, B.-S. Kim, J. Y. Lim, S.-H. Choi, S. J. Ahn, J. R. Ahn, M.-H. Park, C.-W. Yang, B. L. Choi, S.-W. Hwang, and D. Whang, *Science*, **344**, 286 (2014).
17. J. Lahiri, T. Miller, L. Adamska, I. I. Oleynik, and M. Batzill, *Nano Lett.*, **11**, 518 (2011).
18. L. Gao, J. R. Guest, and N. P. Guisinger, *Nano Lett.*, **10**, 3512 (2010).
19. P. Sutter, J. T. Sadowski, and E. Sutter, *Phys. Rev. B*, **80**, 245411 (2009).
20. G. A. Lopéz and E. J. Mittemeijer, *Scr. Mater.*, **51**, 1 (2004).
21. X. Li, W. Cai, L. Colombo, and R. S. Ruoff, *Nano Lett.*, **9**, 4268 (2009).
22. W. Liu, H. Li, C. Xu, Y. Khatami, and K. Banerjee, *Carbon N. Y.*, **49**, 4122 (2011).
23. Y. Zhang, T.-T. Tang, C. Girit, Z. Hao, M. C. Martin, A. Zettl, M. F. Crommie, Y. R. Shen, and F. Wang, *Nature*, **459**, 820 (2009).
24. P. Lespade, A. Marchand, M. Couzi, and F. Cruege, *Carbon N. Y.*, **22**, 375 (1984).
25. Z. Q. Li, C. J. Lu, Z. P. Xia, Y. Zhou, and Z. Luo, *Carbon N. Y.*, **45**, 1686 (2007).
26. S. Shallcross, S. Sharma, E. Kandelaki, and O. A. Pankratov, *Phys. Rev. B*, **81**, 165105 (2010).
27. D. R. Lenski and M.S. Fuhrer, *J. Appl. Phys.*, **110**, 013720 (2011).
28. Y. Shibuta and J. A. Elliott, *Chem. Phys. Lett.*, **512**, 146 (2011).
29. J. M. B. Lopes dos Santos, N. M. R. Peres, and A. H. Castro Neto, *Phys. Rev. Lett.*, **99**, 256802 (2007).
30. W. Wu, Q. Yu, P. Peng, Z. Liu, J. Bao, and S.-S. Pei, *Nanotechnology*, **23**, 035603 (2011).
31. M. Kalbac, O. Frank, and L. Kavan, *Carbon N. Y.*, **50**, 3682 (2012).
32. K. Yan, H. Peng, Y. Zhou, H. Li, and Z. Liu, *Nano Lett.*, **11**, 1106 (2011).
33. Q. Yu, J. Lian, S. Siriponglert, H. Li, Y.P. Chen, and S.S. Pei, *Appl. Phys. Lett.*, **93**, 113103 (2008).
34. T. Yoon, J.H. Mun, B.J. Cho, and T.-S. Kim, *Nanoscale*, **6**, 151 (2014).
35. P. Wu, X. Zhai, Z. Li, and J. Yang, *J. Phys. Chem. C*, **118**, 6201 (2014).
36. B. Wu, D. Geng, Y. Guo, L. Huang, Y. Xue, J. Zheng, J. Chen, G. Yu, Y. Liu, L. Jiang, and W. Hu, *Adv. Mater.*, **23**, 3522 (2011).
37. P. Wu, W. Zhang, Z. Li, J. Yang, and J.G. Hou, *J. Chem. Phys.*, **133**, 171101 (2010).
38. X. Zhang, L. Wang, J.H. Xin, B.I. Yakobson, and F. Ding, *J. Am. Chem. Soc.*, **136**, 3040 (2014).
39. S. Nie, W. Wu, S. Xing, Q. Yu, J. Bao, S.S. Pei, and K.F. McCarty, *New J. Phys.*, **14**, 093028 (2012).
40. K. Verguts, B. Vermeulen, N. Vrancken, K. Schouteden, C. Van Haesendonck, C. Huyghebaert, M. Heyns, S. De Gendt, and S. Brems, *J. Phys. Chem. C*, **120**, 297 (2016).
41. J. W. Suk, A. Kitt, C. W. Magnuson, Y. Hao, S. Ahmed, J. An, A. K. Swan, B. B. Goldberg, and R. S. Ruoff, *ACS Nano*, **5**, 6916 (2011).
42. P. Blake, E. W. Hill, A. H. Castro Neto, K. S. Novoselov, D. Jiang, R. Yang, T. J. Booth, and A. K. Geim, *Appl. Phys. Lett.*, **91**, 063124 (2007).
43. X. Wang, M. Zhao, and D. D. Nolte, *Appl. Phys. Lett.*, **95**, 081102 (2009).
44. A. C. Ferrari and D. M. Basko, *Nat. Nanotechnol.*, **8**, 235 (2013).
45. A. C. Ferrari, *Solid State Commun.*, **143**, 47 (2007).
46. A. C. Ferrari, J. C. Meyer, V. Scardaci, C. Casiraghi, M. Lazzeri, F. Mauri, S. Piscanec, D. Jiang, K. S. Novoselov, S. Roth, and A. K. Geim, *Phys. Rev. Lett.*, **97**, 187401 (2006).
47. D. Nečas and P. Klapetek, *Cent. Eur. J. Phys.*, **10**, 181 (2012).
48. O. Frank, J. Vejpravova, V. Holy, L. Kavan, and M. Kalbac, *Carbon N. Y.*, **68**, 440 (2014).
49. X. Yin, Y. Li, F. Ke, C. Lin, H. Zhao, L. Gan, Z. Luo, R. Zhao, T. F. Heinz, and Z. Hu, *Nano Res.*, **7**, 1613 (2014).
50. D. Graf, F. Molitor, K. Ensslin, C. Stampfer, A. Jungen, C. Hierold, and L. Wirtz, *Nano Lett.*, **7**, 238 (2007).
51. J. D. Wood, G. P. Doidge, E. A. Carrion, J. C. Koepke, J. A. Kaitz, I. Datye, A. Behnam, J. Hewaparakrama, B. Aruin, Y. Chen, H. Dong, R. T. Haasch, J. W. Lyding, and E. Pop, *Nanotechnology*, **26**, 055302 (2015).
52. F. Banhart, J. Kotakoski, and A. V. Krasheninnikov, *ACS Nano*, **5**, 26 (2011).
53. C. Casiraghi, *Phys. Rev. B - Condens. Matter Mater. Phys.*, **80**, 233407 (2009).
54. A. Das, S. Pisana, B. Chakraborty, S. Piscanec, S. K. Saha, U. V Waghmare, K. S. Novoselov, H. R. Krishnamurthy, A. K. Geim, A. C. Ferrari, and A. K. Sood, *Nat. Nanotechnol.*, **3**, 210 (2008).
55. J. A. Venables, G. D. T. Spiller, and M. Hanbücken, *Reports Prog. Phys.*, **47**, 399 (1984).
56. I. Vlassiouk, M. Regmi, P. Fulvio, S. Dai, P. Datskos, G. Eres, and S. Smirnov, *ACS Nano*, **5**, 6069 (2011).
57. B. M. Nichols, *Army Res. Lab.*, (2013).
58. H. Ago, K. Kawahara, Y. Ogawa, S. Tanoue, M. A. Bissett, M. Tsuji, H. Sakaguchi, R. J. Koch, F. Fromm, T. Seyller, K. Komatsu, and K. Tsukagoshi, *Appl. Phys. Express*, **6**, 075101 (2013).
59. F. T. Si, X. W. Zhang, X. Liu, Z. G. Yin, S. G. Zhang, H. L. Gao, and J.J. Dong, *Vacuum*, **86**, 1867 (2012).
60. M. Seifert, S. Drieschner, B.M. Blaschke, L.H. Hess, and J.A. Garrido, *Diam. Relat. Mater.*, **47**, 46 (2014).
61. R. Sandström, Memo 2014-01-27 Contain. Doc. to Be Used Response to Issues Brought up by SSM 1 (2014).
62. A. Dathbun and S. Chaisitsak, *8th Annu. IEEE Int. Conf. Nano/Micro Eng. Mol. Syst. IEEE NEMS 2013*, **1**, 1018 (2013).
63. W. Fang, A.L. Hsu, R. Caudillo, Y. Song, A.G. Birdwell, E. Zakar, M. Kalbac, M. Dubey, T. Palacios, M.S. Dresselhaus, P.T. Araujo, and J. Kong, *Nano Lett.*, **13**, 1541 (2013).
64. Y. Wang, Z. Su, W. Wu, S. Nie, X. Lu, H. Wang, K. McCarty, S. Pei, F. Robles-Hernandez, V. G. Hadjiev, and J. Bao, *Nanotechnology*, **25**, 335201 (2014).